Supplementary file

Geological CO_2 storage in heterogeneous saline aquifers: Insights into the mechanisms of thermal and density effects

Aohan Jin[1], Eungyu Park[2], Cai Li[3], Wenguang Shi[1], Quanrong Wang[1, 4*]

[1]*School of Environmental Studies, China University of Geosciences, Wuhan 430074, P. R. China*

[2]*Department of Geology, Kyungpook National University, Daegu 41566, Republic of Korea*

[3]*Hainan Branch, CNOOC(China) Limited, Haikou 570100, P. R. China*

[4]*MOE Key Laboratory of Groundwater Quality and Health, China University of Geosciences, Wuhan 430078, P. R. China*

E-mail address: ahjin@cug.edu.cn (A. Jin); egpark@knu.ac.kr (E. Park); licai1@cnooc.com.cn (C. Li); swg@cug.edu.cn (W. Shi); wangqr@cug.edu.cn (Q. Wang);

[*]Corresponding author (ORCID: 0000-0002-6560-6340 (Q. Wang))

Jin, A., Park, E., Li, C., et al. Geological CO_2 storage in heterogeneous saline aquifers: Insights into the mechanisms of thermal and density effects. Advances in Geo-Energy Research, 2026, 19(3): 216-230.

The link to this file is: https://doi.org/10.46690/ager.2026.03.02

Appendix A: Effect of structural deformation and thermal effect on pore pressure field

The continuity equation for groundwater problems based on the storage coefficient can be written as follows:

$$\rho_f S \frac{\partial p}{\partial t} + \nabla \cdot \left(\rho_f u \right) = Q_m \tag{S1}$$

$$u = -\frac{K}{\mu}(\nabla p - \rho_f g) \tag{S2}$$

$$S = \phi c_f + (1-\phi) c_s \tag{S3}$$

where ρ_f is the fluid density (kg/m^3); ϕ is the porosity (-); t is time (s); Q_m is the mass source/sink term (kg/m^3/s); u is the Darcy's velocity (m/s); K is the permeability tensor of the porous media (m^2); μ is the fluid (Pa·s); p is the fluid pressure (Pa); g is the gravity acceleration (m/s^2); S is the storage coefficient of the porous media (-); c_f and c_s are the compression coefficients (1/Pa) of fluid and solid phases, respectively.

In addition, based on the principles of pore elasticity, when coupling fluid flow with solid deformation processes, the increase in fluid content can be attributed to the volumetric strain of the porous matrix (Biot, 1962):

$$\zeta = \frac{\partial p}{M} + b\varepsilon_{vol} = \frac{\partial(\rho_f \phi)}{\rho_f} \tag{S4}$$

where ζ is the fluid content increase (-); $M = 1/S$ is the Boit modulus (Pa), b is the Boit coefficient (-); ε_{vol} is the volumetric strain (-).

Substituting Eq. (S4) into Eq. (S1), one can obtain:

$$\rho_f S \frac{\partial p}{\partial t} + \nabla \cdot \left(\rho_f u \right) = Q_m - b\rho_f \frac{\partial \varepsilon_{vol}}{\partial t} \tag{S5}$$

Furthermore, when thermal effects are considered, the continuity equation is established according to the principles of thermal pore elasticity theory (Li et al., 2016):

$$\rho_f S \frac{\partial p}{\partial t} + \nabla \cdot \left(\rho_f u \right) = Q_m - b\rho_f \frac{\partial \varepsilon_{vol}}{\partial t} + 3\rho_f \alpha_T \frac{\partial T}{\partial t} \tag{S6}$$

where T is the temperature (K); α_T is the linear thermal expansion coefficient of rock mass (1/K), which is defined as $\alpha_T = (1-\phi)\alpha_s + \phi\alpha_f$; α_s and α_f are the linear thermal expansion coefficients of the solid skeleton and fluid (1/K), respectively.

Appendix B: Porosity evolution model with thermal effects

The injection of CO_2 leads to alterations in fluid pressure and reservoir temperature, thereby inducing compressive and thermal deformation of the solid skeleton. According to the definition of porosity, it can be known that:

$$\mathrm{d}\phi = \mathrm{d}\left(\frac{V_P}{V_B}\right) = \mathrm{d}\left(1-\frac{V_S}{V_B}\right) = -\frac{\mathrm{d}V_S}{V_B} + \frac{V_S}{V_B}\times\frac{\mathrm{d}V_B}{V_B} = -\frac{V_S}{V_B}\times\frac{\mathrm{d}V_S}{V_S} + \frac{V_S}{V_B}\times\frac{\mathrm{d}V_B}{V_B} = -(1-\phi)\times\frac{\mathrm{d}V_S}{V_S} + (1-\phi)\times\frac{\mathrm{d}V_B}{V_B} \quad \text{(S7)}$$

$$\frac{1}{1-\phi}\mathrm{d}\phi = -\frac{\mathrm{d}V_S}{V_S} + \frac{\mathrm{d}V_B}{V_B} \quad \text{(S8)}$$

where ϕ is the porosity (-); V_B, V_S and V_P are the rock, skeleton and pore volume (m^3), respectively. In Eq. (S8), the first term on the right side represents the strain increment of the solid skeleton, and the second term represents the overall strain increment.

The strain increment in the solid skeleton arises from two primary mechanisms: solid skeleton compression induced by fluid pressure variations and thermoelastic expansion due to temperature changes.

$$\frac{\mathrm{d}V_S}{V_S} = \frac{\mathrm{d}V_{SP}}{V_S} + \frac{\mathrm{d}V_{ST}}{V_S} \quad \text{(S9)}$$

$$\frac{\mathrm{d}V_{SP}}{V_S} = \frac{1}{K_s}\mathrm{d}p \quad \text{(S10)}$$

$$\frac{\mathrm{d}V_{ST}}{V_S} = \alpha_T \mathrm{d}T \quad \text{(S11)}$$

$$\frac{\mathrm{d}V_S}{V_S} = -\frac{1}{K_s}\mathrm{d}p + \alpha_T \mathrm{d}T \quad \text{(S12)}$$

where K_S is the solid skeleton modulus (Pa), α_T is the linear thermal expansion coefficient of the rock mass (1/K). The overall strain increment can be expressed as:

$$\frac{\mathrm{d}V_B}{V_B} = \mathrm{d}\varepsilon_{vol} \quad \text{(S13)}$$

Substituting Eqs. (S12) and (S13) into Eq. (S8), one can obtain:

$$\frac{1}{1-\phi}\mathrm{d}\phi = \frac{1}{K_s}\mathrm{d}p - \alpha_T \mathrm{d}T + \mathrm{d}\varepsilon_{vol} \quad \text{(S14)}$$

Integrating both sides of Eq. (S14), one can obtain:

$$\int_{\phi_0}^{\phi} \frac{1}{1-\phi}\,\mathrm{d}\phi = \int_{p_0}^{p} \frac{1}{K_s}\,\mathrm{d}p - \int_{T_0}^{T} \alpha_T\,\mathrm{d}T + \int_{\varepsilon_{vol_0}}^{\varepsilon_{vol}} \mathrm{d}\varepsilon_{vol} \tag{S15}$$

$$\ln\left(\frac{1-\phi_0}{1-\phi}\right) = \frac{1}{K_s}\left(p - p_0\right) - \alpha_T\left(T - T_0\right) + \left(\varepsilon_{vol} - \varepsilon_{vol_0}\right) \tag{S16}$$

$$\phi = 1 - (1-\phi_0)\exp\left[-\frac{1}{K_s}\left(p - p_0\right) + \alpha_T\left(T - T_0\right) - \left(\varepsilon_{vol} - \varepsilon_{vol_0}\right)\right] \tag{S17}$$

Appendix C: Benchmark analytical solution proposed by Liu et al. (2018)

Based on the assumption that the change of the void ratio is caused by effective stress, creep effect and temperature, a one-dimensional nonlinear consolidation theory considering the thermal effect is established by Liu et al. (2018). They derived analytical solutions for a one-dimensional nonlinear thermal consolidation problem with and without secondary consolidation. The detailed derivation process can be found in Liu et al. (2018). In this section, a one-dimensional nonlinear thermal consolidation solution that neglects secondary consolidation is used as the benchmark to validate the effectiveness of the proposed coupled THM model. The solutions for pore pressure and average degree of consolidation are listed as follows:

$$u=\sigma_f^{'}\left\{1-\exp\left[\sum_{n=1}^{\infty}\sin\frac{Mz}{H}\exp\left(-\frac{a^2M^2}{H^2}t\right)\left[\sum_{n=1}^{\infty}\frac{2\alpha_T C_e M\left(1+e1\right)\ln 10}{H^2\lambda_e C_p}\cdot T_s\int_0^t\exp\left(\frac{\lambda_e a^2-C_e}{\lambda_e H^2}M^2\tau\right)\mathrm{d}\tau+\frac{2}{M}\ln\frac{\sigma_0^{'}}{\sigma_f^{'}}\right]\right]\right\} \tag{S18}$$

$$U=1-\frac{1}{\log\frac{\sigma_f^{'}}{\sigma_0^{'}}}\sum_{n=1}^{\infty}\frac{1}{M\ln 10}\exp\left(-\frac{a^2M^2}{H^2}t\right)\left[-\int_0^t\sum_{n=1}^{\infty}\frac{2\alpha_T C_e M\left(1+e1\right)\ln 10}{H^2\lambda_e C_p}\cdot T_s\exp\left(-\frac{M^2}{H^2}(\frac{C_e}{\lambda_e}-a^2)\tau\right)\mathrm{d}\tau-\frac{2}{M}\ln\frac{\sigma_0^{'}}{\sigma_f^{'}}\right] \tag{S19}$$

$$M=\frac{(2n-1)\pi}{2},\ n=1,2,3\mathrm{L} \tag{S20}$$

$$C_e=\left(1-n\right)\rho_r C_{pr}+n\rho_w C_{pw} \tag{S21}$$

$$\lambda_e=\left(1-n\right)\lambda_r+n\lambda_w \tag{S22}$$

$$B=\frac{\sigma_0^{'}k_{v0}\left(1+e1\right)\ln 10}{r_w} \tag{S23}$$

$$a^2=\frac{B}{C_p} \tag{S24}$$

where H is the thickness of the formation (m); C_e is the effective heat capacity (J/(m^3·K)); C_p is the compressive index of effective stress change (-); λ_e is the effective thermal conductivity of the formation (W/(m·K)); n is the porosity of the formation (-); ρ_r and ρ_w are the densities of the solid matrix and water (kg/m^3), respectively; C_{pr} and C_{pw} are the specific heat capacities of the solid matrix and water (J/(kg·K)), respectively; λ_r and λ_w are the thermal conductivities of the solid matrix and water (W/(m·K)), respectively; T_s is the temperature increment; σ_0' is the initial effective stress (Pa); σ_f' is the final effective stress

(Pa); α is the linear expansion coefficient of the soil skeleton (1/K); $e1$ is the initial void ratio (-); k_{v0} is the initial permeability coefficient (-).

Table S1. Basic parameters used for numerical model verification

Parameter	Value	Description
H	1 m	Depth
k_{v0}	1e-8 m/s	Initial permeability coefficient
σ_f'	101 kPa	Ultimate effective stress
σ_0'	1 kPa	Initial effective stress
$e1$	1.2	Initial void ratio
C_p	0.3	Compressive index of effective stress change
α_T	2e-5 1/K	Thermal expansion coefficient of rock
C_{pr}	874 J/kg/K	Specific heat capacity of rock
C_{pw}	4,200 J/kg/K	Specific heat capacity of water
n	0.545	Initial porosity
ρ_w	1,000 kg/m^3	Density of water
ρ_r	2,600 kg/m^3	Density of solid matrix
λ_r	1.5 W/m/K	Thermal conductivity of solid matrix
λ_w	0.59 W/m/K	Thermal conductivity of water

Appendix D: Supplementary figures

Fig. S1 shows the spatial distribution of pore pressure for both low- and high-permeability cases, and the corresponding volumetric-strain field is presented in Fig. S2. It can be observed that low-permeability cases show a more gradual pressure decay, whereas high-permeability cases exhibit a rapid transition to the baseline pressure. The volumetric-strain distributions display a similar pattern, with low-permeability cases exhibiting larger overall strain magnitudes than high-permeability cases. This disparity highlights that restricted fluid mobility impedes pore-pressure dissipation, thereby promoting consolidation and mechanical deformation under low-permeability conditions.

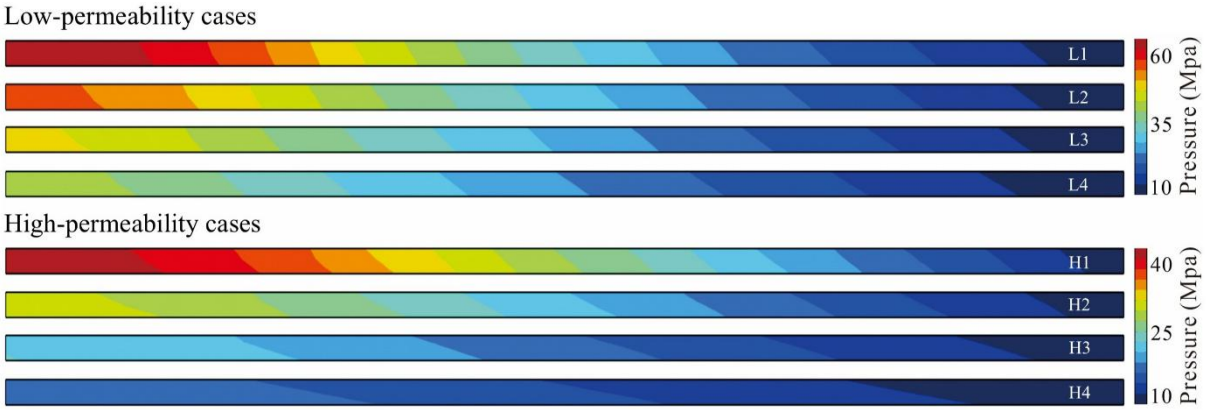

Fig. S1. Spatial distribution of pressure under different heterogeneous conditions.

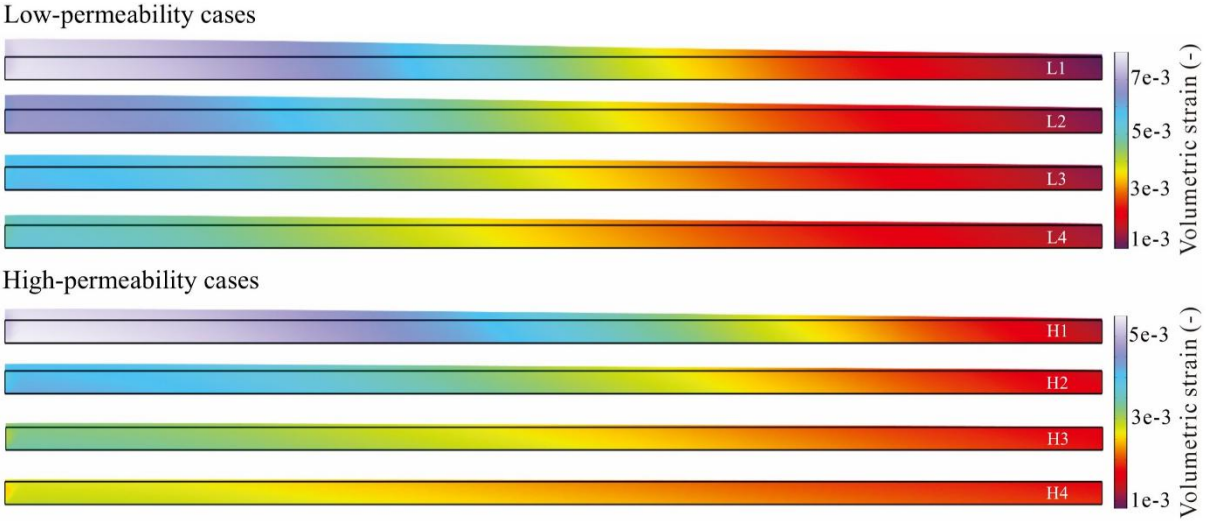

Fig. S2. Spatial distribution of volumetric strain under different heterogeneous conditions.

Fig. S3 shows the corresponding distribution of thermal deformation, which exhibits consistent patterns with those observed in Fig. 8. The range of thermal deformation is limited to approximately 100 m. Similarly, preferential flow pathways are formed in high-permeability scenarios, as indicated by the black circle in Fig. S3.

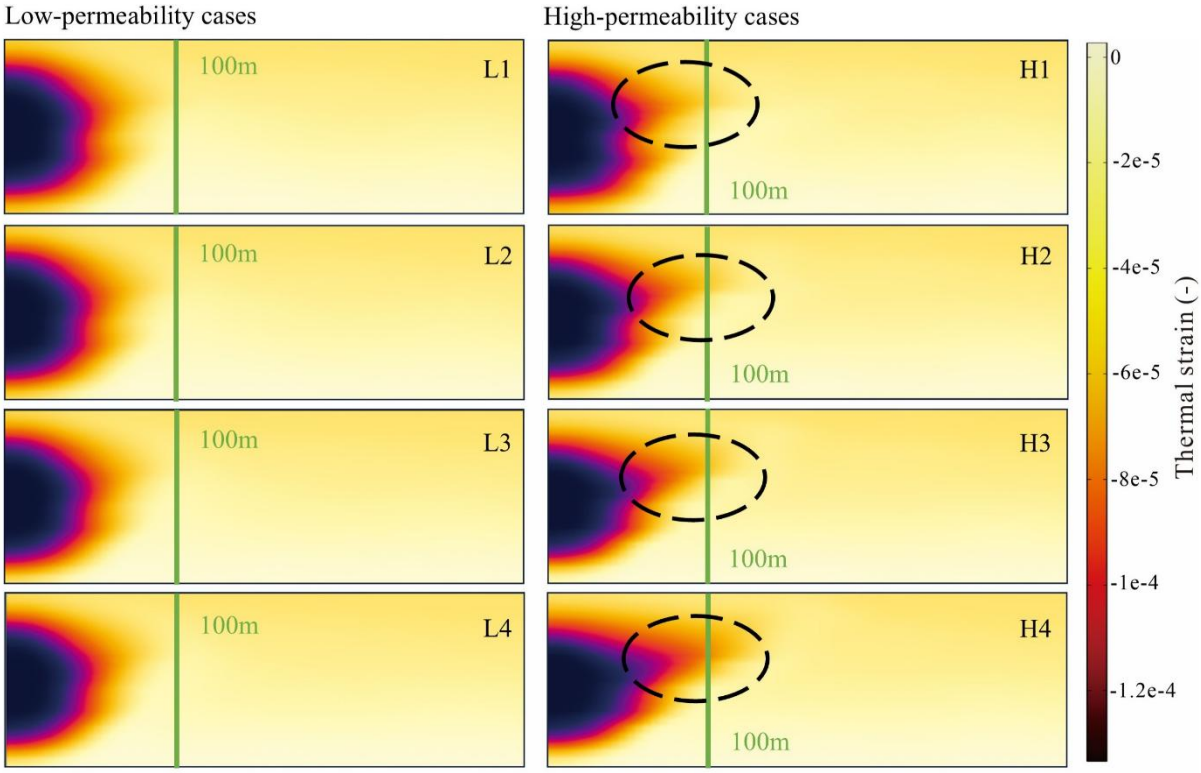

Fig. S3. Spatial distribution of thermal deformation under different heterogeneous conditions.

Figs. S4 and S5 show the temporal evolution of CO_2 fingers in both low- and high-permeability reservoirs. It can be observed that, in high-permeability reservoirs, vigorous convective fingers are fully established within a relatively short period (after only 50 years), whereas the low-permeability scenarios require up to 200 years to attain a comparable plume depth. Additionally, in high-permeability scenarios, higher Ra numbers lead to thin, distinct fingers with complex branching and merging behaviors, that facilitate the rapid vertical mass transfer of the CO_2-saturated brine. While in the low-permeability scenarios, the fingers appear coarser, thicker, and sparser, and the interface between the diffusive boundary layer and the underlying brine remains relatively smooth (particularly in Case L1), indicating that the diffusive mechanism still plays a significant role.

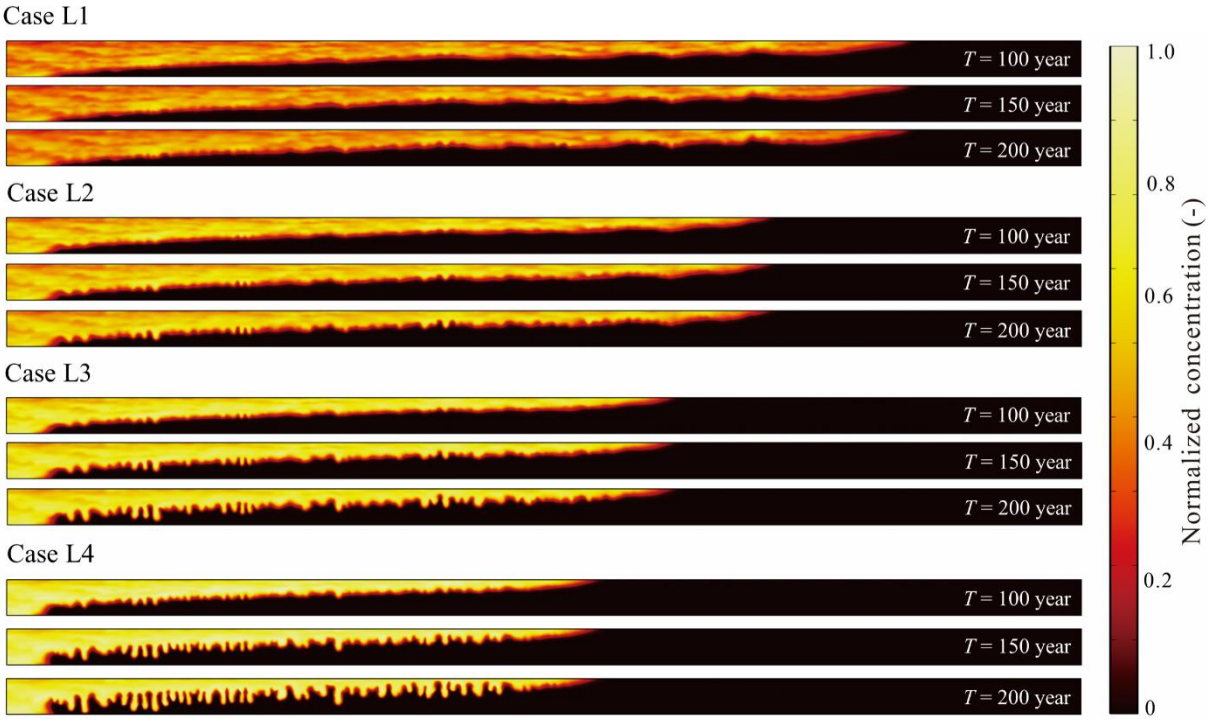

Fig. S4. Temporal evolution of CO_2 fingers in low-permeability reservoirs.

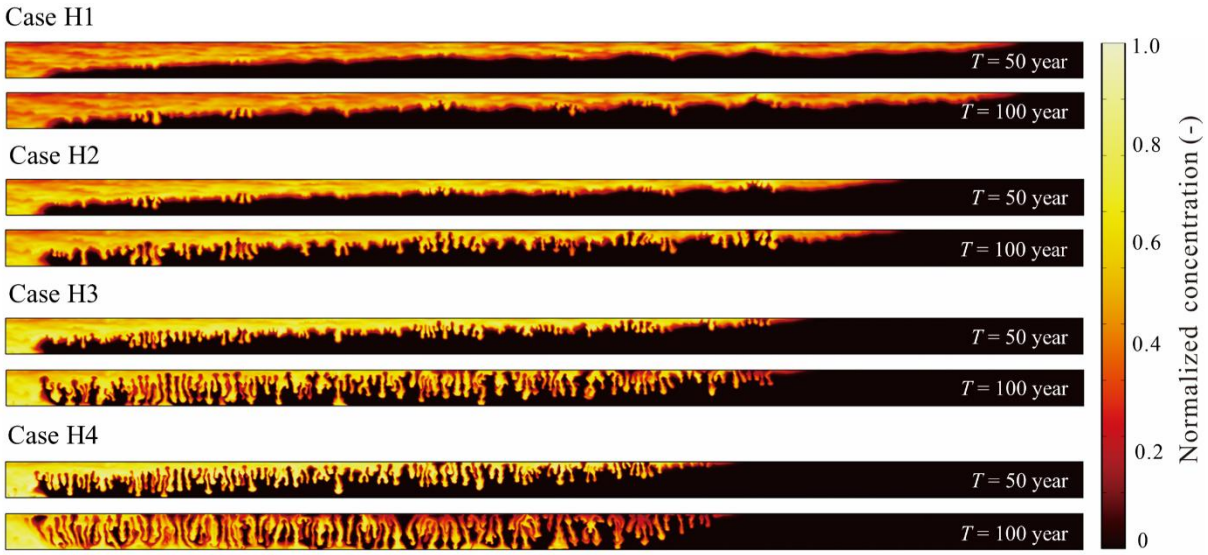

Fig. S5. Temporal evolution of CO_2 fingers in high-permeability reservoirs.

Reference

Biot, M. A. Mechanics of deformation and acoustic propagation in porous media. Journal of Applied Physics, 1962, 33(4): 1482-1498.

Li, S., Li, X., Zhang, D. A fully coupled thermo-hydro-mechanical, three-dimensional model for hydraulic stimulation treatments. Journal of Natural Gas Science and Engineering, 2016, 34: 64-84.

Liu, Q., Deng, Y., Wang, T. One-dimensional nonlinear consolidation theory for soft ground considering secondary consolidation and the thermal effect. Computers and Geotechnics, 2018, 104: 22-28.